



Cite this: DOI: 10.1039/c5cp02931g

# A means to an interface: investigating monoethanolamine behavior at an aqueous surface†

Laura E. McWilliams, Nicholas A. Valley, Sumi N. Wren and Geraldine L. Richmond\*

The use of amine scrubbers to trap carbon dioxide from flue gas streams is one of the most promising avenues for atmospheric carbon dioxide reduction. However, modifications are necessary to efficiently scale these scrubbers for use in fossil fuel plants. Current advances in tailoring amines for CO<sub>2</sub> capture involve improvements of bulk kinetic and thermodynamic parameters, with little consideration to surface chemistry and behavior. Aqueous alkanolamine solutions, such as monoethanolamine (MEA), are currently highly favored sorbents in CO<sub>2</sub> post-combustion capture. Although numerous studies have explored MEA–CO<sub>2</sub> chemistry at the macroscopic scale, few have investigated the role of the interface in the gas adsorption process. Additionally, as these amines become more industrially ubiquitous, their presence on and the need to understand their behavior at atmospheric and environmental surfaces will increase. This study investigates the surface behavior of monoethanolamine at the vapor/water interface, with particular focus on MEA's surface orientation and footprint. Using vibrational sum frequency spectroscopy, surface tensiometry, and computational techniques, MEA is found to adopt a constrained gauche interfacial conformation with its methylene backbone oriented toward the vapor phase and its functional groups solvated in the bulk solution. Computational and experimental analysis agree well, giving a complete picture with vibrational mode assignments and surface orientation of MEA. These findings can assist in the tailoring of amine structures or to facilitate improvements in engineering design to exploit favorable surface chemistry, as well as to serve as a starting point toward understanding aqueous amine surface behavior relevant to environmental systems.

Received 21st May 2015,  
Accepted 22nd July 2015

DOI: 10.1039/c5cp02931g

www.rsc.org/pccp

## 1 Introduction

CO<sub>2</sub>(g) has long been implicated in climate change, with fossil fuel burning being its major anthropogenic source.<sup>1–4</sup> Technologies capable of removing CO<sub>2</sub> efficiently and economically from fossil fuel exhaust streams are critical,<sup>5</sup> as fossil fuels currently supply ~85% of U.S. energy consumption.<sup>6</sup> While many carbon capture and storage (CCS) technologies exist, post-combustion CO<sub>2</sub> capture is considered more economically feasible and scalable,<sup>7,8</sup> as the majority (~60%) of global CO<sub>2</sub> emissions arise from stationary sources.<sup>1</sup> Post-combustion CCS technologies retrofit existing power plants by enabling end-of-stream capture in

flue lines. These technologies employ different combinations of capture materials (reactive substrates or sorbents, such as liquid amines) and/or reactor designs (flow cells, reactor beds).

At present, aqueous amines are a leading candidate for CCS post-combustion scrubbing processes.<sup>8</sup> The amine scrubbers exploit an exothermic ( $\Delta H_f \sim -7.1 \text{ kcal mol}^{-1}$ )<sup>9</sup> reaction between gaseous CO<sub>2</sub> and aqueous amines (or amine-functionalized solid sorbents) to generate carbamate or carbamic acid products. The amines are commonly introduced to the gaseous exhaust stream as an aqueous spray, reacting with CO<sub>2</sub> in the liquid. The CO<sub>2</sub>–MEA reaction product remains in the liquid, which is collected and sent to a heated stripper unit. In the stripper unit, the CO<sub>2</sub> is separated from the amine, allowing the amine to then be recycled back into the exhaust stream.<sup>7</sup>

Monoethanolamine (“MEA”; HO(CH<sub>2</sub>)<sub>2</sub>NH<sub>2</sub>), a low molecular weight amine (Fig. 1), is the current benchmark molecule for post-combustion CCS, in part due to its ease of manufacture and low cost.<sup>10</sup> It is currently used in the natural gas industry to scrub CO<sub>2</sub> from flue lines.<sup>7</sup> Despite its prominence, MEA has a number of shortcomings (corrosiveness, input energy for CO<sub>2</sub> stripping, *etc.*) that make its implementation in power plants prohibitive.<sup>3,6,8</sup>

Department of Chemistry, University of Oregon, Eugene, OR, 97403 USA.

E-mail: richmond@uoregon.edu; Tel: +1 541 346 4648

† Electronic supplementary information (ESI) available: Discussion of xc-functional and basis sets used for DFT calculations, with comparative spectra. Evaluation of static DFT structures and matching of DFT structures with MD conformers. Spectra of deuterated 10 M MEA in bending region. Plots of MEA surface pressure and surface excess. Calculations of surface mole fraction from surface pressure data, with necessary plots. Calculation of average molecular tilt from ssp methylene intensities. See DOI: 10.1039/c5cp02931g

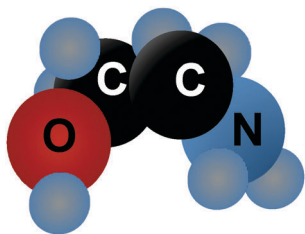


Fig. 1 Representation of monoethanolamine; "MEA".

Consequently, there has been demand for new and efficient sorbent materials for CO<sub>2</sub> capture. Proposed materials currently include novel amines or hydroxides, ionic liquids,<sup>11,12</sup> amine-tethered metal-organic frameworks, functionalized polymers, as well as zeolite membranes.<sup>3,4</sup> While many molecular techniques have been employed to probe the interactions between these sorbents and CO<sub>2</sub>, few studies have considered the role the aqueous solution surface (or solid membrane surface) plays in CO<sub>2</sub> capture from scrubbers. The successful design and development of these materials ultimately rests on a good physical and chemical understanding of the uptake and reactivity of CO<sub>2</sub> with these substrates. Thus this lack of understanding of the surface behavior of these amine technologies is an oversight for a few reasons. Firstly, these sorbent materials have chemical components (such as polymers<sup>13,14</sup> or ionic liquids<sup>15–18</sup>) known to have different orientations, speciation and behavior at surfaces compared to bulk solution. Secondly, as the first point of contact of the gas entering the condensed phase, the surfaces of these materials could be utilized to better facilitate gas uptake.

In fact, recent soft-X-ray photoelectron spectroscopy (PES) measurements of aqueous MEA and CO<sub>2</sub>-treated aqueous MEA solutions have alluded to the surface's role in CO<sub>2</sub> uptake chemistry. MEA-CO<sub>2</sub> chemistry was suggested to be facilitated by the interface, with reactants and products showing different bulk *vs.* surface partitioning.<sup>19,20</sup> In a second X-ray PES study, amine-functionalized ionic liquids (AFILs) also showed unique surface behavior. Not only did the AFILs show faster absorption and reaction of CO<sub>2</sub> at the surface relative to diffusion and reaction in the bulk, but the AFILs also reacted at the surface *via* a different pathway than the bulk.<sup>21</sup> Yet, the reasons for this difference in surface *vs.* bulk behavior are not fully understood or characterized.

In tandem with these chemical advances, novel engineering strategies are also beginning to exploit the surface. In rotating packed beds, for example, the amine solution is formed into small droplets or thin films under high centrifugal force, causing the gas-liquid contact area and mass transfer rates to increase significantly.<sup>8,22,23</sup> Further exploiting these differences in surface *vs.* bulk behavior for post-combustion CO<sub>2</sub> capture requires a detailed molecular level understanding of the surface adsorption and coverage of proposed sorbent materials.

Furthermore, understanding these amines on aqueous surfaces warrants extensive study due to emissions concerns of the amine sorbents themselves. For instance, gas power plants emitting ~1 million tons CO<sub>2</sub> per year are estimated to emit

40–160 tons of amines per year to the atmosphere, assuming use of current CCS technologies.<sup>24</sup> This level of increase in atmospheric amine concentrations could have a dramatic impact on atmospheric chemistry, particularly in condensed phases such as clouds and aerosol surfaces where these highly water soluble amines are likely to reside.<sup>25</sup> Despite these concerns, little is known regarding amine atmospheric chemistry, especially amine gas to particle partitioning.<sup>26</sup> Recent studies have been attempting to close this knowledge gap, examining gaseous oxidation of MEA,<sup>27,28</sup> ammonium salt formation *via* amine chemistry on sulfuric acid/sulfate particles,<sup>29</sup> new particle growth from similar sulfuric acid spray,<sup>30</sup> as well as toxic nitrosamine formation from photooxidation of amines in the presence of NO<sub>x</sub>.<sup>31</sup> However, more studies are necessary to fully understand and model the complex chemistry of these amines in the atmosphere, especially on aqueous surfaces.

To provide new insights into the molecular nature of amine interfacial adsorption, this study uses a unique approach that combines surface vibrational spectroscopy, surface interfacial tensiometry and computational methodology. The system chosen for examination is MEA, the benchmark chemical of CCS. This study provides much needed information about the surface adsorption, orientation, and conformation of MEA at the air/water interface. The new insights gained are important for future CCS design as well as for understanding the behavior of amines on atmospheric aqueous surfaces. This study also further validates the computational methodology for obtaining a detailed picture of surface vibrational spectra and behavior.

## 2 Experimental details

### 2.1 Surface spectroscopy background

Many techniques exist to study chemistry in the bulk, yet few can sensitively probe molecular properties at an interface. Vibrational sum frequency spectroscopy (VSFS) is ideal for studying molecular interfacial properties, as the symmetry of the liquid surface causes VSFS to only probe molecules within a few Angstroms of the interface. Notable contributions detailing VSFS at liquid surfaces exist in the literature,<sup>32–37</sup> such that only a brief description of the theory relevant to these studies is necessary.

In VSFS, incident visible and infrared beams (IR) overlap at an interface and generate an output beam (SF) that oscillates at the sum of the two incident frequencies. The intensity of the SF light is enhanced when the IR frequency is resonant with molecular vibrational modes. Thus, by tuning the IR beam across a wavelength range, VSFS generates a vibrational spectrum of interfacial molecules. The intensity of the SF beam is proportional to the intensities of the incident IR and visible beams and the square of the second-order nonlinear susceptibility,  $\chi^{(2)}$ , which contains both resonant,  $\chi_{R,}^{(2)}$ , and nonresonant,  $\chi_{NR,}^{(2)}$ , terms. Spectra must be fit to deconvolve the nonresonant response and the individual resonant modes. A fitting routine,<sup>38,39</sup> based on eqn (1), is, employed to deconvolve these spectral contributions and to account for both homogeneous ( $\Gamma_1$ ) and

inhomogeneous ( $\Gamma_\nu$ ) broadening of the individual vibrational transitions.

$$\chi^{(2)} = \chi_{\text{NR}}^{(2)} e^{i\psi} + \sum_{\nu} \frac{A_{\nu} e^{i\phi_{\nu}} e^{-[(\omega_L - \omega_{\nu})/\Gamma_{\nu}]^2}}{\omega_L - \omega_{\text{IR}} + i\Gamma_L} \quad (1)$$

The first term in eqn (1) accounts for the non-resonant contributions to the VSF spectra, including the non-resonant amplitude and phase ( $\psi$ ). The second term in eqn (1) is a sum over all the resonant modes  $\chi_{\text{R}\nu}^{(2)}$ .  $\chi_{\text{R}\nu}^{(2)}$  depends on both the orientational average of the molecular hyperpolarizabilities,  $\langle\beta\rangle$ , and the number of contributing molecules,  $N$ , *via* eqn (2). This relationship indicates an important aspect of VSFS: the measured signal is due to both population and orientation at the interface.

$$\chi_{\text{R}\nu}^{(2)} = \frac{N}{\epsilon_0} \langle\beta_{\nu}\rangle \quad (2)$$

In VSFS, the nonlinear susceptibility term,  $\chi^{(2)}$ , may be probed by unique polarization schemes. Polarizations such as ssp and sps are common in VSFS, where  $p$  and  $s$  refer to the orientation of the polarized  $\mathbf{E}$  fields relative to the plane of incidence. Polarization designations are given to the incident and outgoing beams in energetic order: SF, visible, IR. A simplistic way to interpret these polarization schemes in regard to the VSFS spectra is that sps probes the component of dipole moments in the plane of the interface, while ssp probes those components normal to the interface.

Spectral fits for the neat air/water interface in both ssp- and sps-polarization schemes have been well established in the literature.<sup>40–43</sup> The fitting routine employed in these studies is nontrivial, as shown by eqn (1), and contains contributions from the vibrational transition strengths ( $A_{\nu}$ ), phases ( $\phi_{\nu}$ ), peak frequencies ( $\omega_{\nu}$ ), and broadening terms ( $\Gamma_{\nu}$  and  $\Gamma_L$ ) of all resonant modes. The broadening due to line widths of the individual molecular transitions ( $\Gamma_L$ ) are fit to either 2  $\text{cm}^{-1}$  (CHs), 5  $\text{cm}^{-1}$  (coordinated OHs), 7  $\text{cm}^{-1}$  (NHs), or 12  $\text{cm}^{-1}$  (free OH) based on reported vibrational relaxation lifetimes of the specific transition.<sup>44–48</sup> Global fitting routines were used when possible to allow for more confidence in the spectral interpretation. Reasonable global fits were achieved by allowing amplitudes of resonant modes to vary with all other peak contributions held constant.

## 2.2 Laser system

The laser system used in this study has been extensively described in a prior publication,<sup>49</sup> such that only a brief description is necessary here. After shaping the incident laser pulses using a combination of Ti:Sapphire oscillator and amplifier systems, the resultant  $\sim 2.6$  ps beam is  $\sim 2$  W centered at 800 nm with a 1 kHz repetition rate. A quarter of the  $\sim 2$  W is then split to form the visible beam used in the sum frequency studies, while the remaining three quarters is directed into an optical parametric amplifier/difference frequency generator system (TOPAS/nDFG by Light Conversion) to produce the IR beam. This IR beam ranges from  $\sim 4000$  ( $\sim 25$   $\mu\text{J}$ ) to 800  $\text{cm}^{-1}$  ( $\sim 2$   $\mu\text{J}$ ).

The spectra presented here were obtained in either the ssp- or sps-polarization schemes. The IR and visible beams are overlapped at the sample surface, and the reflected SF signal is monitored using a thermoelectrically cooled CCD camera (Princeton Instruments). Incident angles of the visible and IR beams were fixed at 45° and 60°, respectively, from surface normal in a copropagating geometry for the majority of experiments presented here. For the polarization study, incident angles were fixed at 63° and 55°, respectively, across all polarizations in order to acquire more favorable SF intensity. Spectra were collected using a LabView program that records CCD intensity at every wavelength step (3  $\text{cm}^{-1}$ ) over the tunable range. The absorption of a polystyrene standard was measured daily and used to calibrate the recorded wavelengths of the infrared beam. Spectra presented here are averages of 6–18 spectra taken over multiple days to ensure reproducibility in the spectral response and to minimize contributions from the background. Additionally, the nonresonant sum frequency response of an uncoated gold substrate was measured before each data set, and used to normalize the experimental spectra. Spectra of the neat air/water interface were also acquired during each data set to ensure spectral intensities were comparable. All measurements were acquired at room temperature ( $\sim 20$  °C) in a purged air environment ( $< 30\%$  RH *via* a Parker Domnick Hunter Pseudri MiDAS).

## 2.3 Surface tension

Surface tension data were collected using the Wilhelmy plate method<sup>50</sup> *via* a force balance (KSV Instruments). Samples were held in clean glass dishes, and a platinum plate (Biolin Scientific) connected to the force balance was carefully lowered into the solution. The platinum plate was thoroughly rinsed in  $> 18$  M $\Omega$  cm nanopure water and heated under flame until glowing orange before each measurement was taken. Surface tension of the neat air/water interface was taken at the start of data collection to ensure surface tension values for each data set were comparable. Surface tension values were corrected for instrumental fluctuations by subtracting the surface tension of the neat air/water surface to generate surface pressure values. All measurements were recorded at room temperature ( $\sim 20$  °C).

## 2.4 Sample preparation

Monoethanolamine ( $\geq 99\%$ ) was purchased from Sigma-Aldrich. All solutions (0.1–10 M) were diluted volumetrically with either H<sub>2</sub>O ( $> 18$  M $\Omega$  cm, Barnstead E-pure) or D<sub>2</sub>O ( $\geq 99.9\%$ , Cambridge Isotopes), and sonicated for a minimum of 10 minutes before use. All solutions were examined at their native pH; for monoethanolamine this corresponds to pH  $\sim 12.5$ . All glassware was scrupulously cleaned for a minimum of 24 hours in a sulfuric acid-NoChromix bath before being thoroughly rinsed under  $> 18$  M $\Omega$  cm nanopure water and dried in a  $> 240$  °C oven.

## 2.5 Computational methods

The computational methodology used in this study has been outlined in previous publications,<sup>13,49,51–53</sup> and is discussed here as it applies to this work.

**2.5.1 Classical molecular dynamics.** Classical molecular dynamics (MD) simulations were performed using the Amber 12 suite of programs,<sup>54</sup> with starting configurations created in PACKMOL.<sup>55</sup> Parameters and force fields were generated as in previous studies.<sup>51,52</sup> An *NVT* ensemble was used, with the simulations performed using a time step of 1 fs. Energy minimization of the initial system at 0 K, equilibration of the system from 0 K to 298 K, and evolution of the system also employed methods outlined in previous studies.<sup>49,52</sup> The system temperature was maintained during the evolutions *via* Langevin dynamics with a leapfrog integrator. Data were extracted from the MD simulations after a minimum of 50 ns of evolution. Monoethanolamine configurations consisted of 80 or 160 MEA molecules with 900 water molecules in a 30 Å cube, roughly corresponding to total concentrations of ~5 M and ~10 M MEA, respectively. Interfaces were created by expanding one dimension of the cube to 120 Å and applying periodic boundary conditions. The interface was defined by the Gibbs dividing surface, and data were collected for both vacuum/water interfaces of the box. Distances are reported relative to the interface and bond angles are reported relative to the surface normal pointing into the vacuum.

**2.5.2 Quantum mechanical calculations.** Density functional theory (DFT) calculations were performed using the NWChem<sup>56</sup> and Gaussian 09<sup>57</sup> program packages. Geometry optimization and harmonic frequency calculations for isolated gas phase amine molecules were performed using the B3LYP exchange–correlation functional and the 6-311++G(2d,2p) basis set. Anharmonic corrections to vibrational frequencies were afforded by second-order vibrational perturbation theory (VPT2). A range of combinations was explored in order to determine the best agreement between the calculated and experimental VSF spectra, with selection of basis sets and functionals guided by literature precedent.<sup>58–61</sup> B3LYP, B2PLYP, and MP2 xc-functionals were matched with either 6-311++G(2d,2p) or aug-cc-pVTZ basis sets.

Ultimately B2PLYP/6-311++G(2d,2p) was found to provide the best agreement between calculated and experimental VSF spectra with respect to both peak positions and relative intensities; a discussion of these tested methodologies is found in the ESI.†

VSF intensities were calculated using in-house code<sup>53</sup> that probes the second-order linear susceptibility tensor *via* eqn (3).

$$\chi_{ijk}^{(2)} \propto \sum_{a,b,c} C_{abc} \frac{\partial \alpha_{ab}}{\partial Q_q} \frac{\partial \mu_c}{\partial Q_q} \quad (3)$$

Polarizability ( $\alpha$ ) and dipole moment ( $\mu$ ) derivatives were calculated using three-point finite differentiation with respect to the displacement of the normal mode  $q$  ( $\partial Q_q$ ), while the laboratory and molecular reference frames were related *via*  $C_{abc}$ . This methodology allows matching of the static gas phase DFT structures with the molecular orientations and conformations acquired in the MD simulations. A discussion of the DFT structures used in the calculations is found in the ESI.† Spectra were empirically broadened using Lorentzian and Gaussian widths comparable to the experimental spectral fits.

## 3 Results and discussion

### 3.1 Experimental VSF spectra

Fig. 2 shows vibrational sum frequency spectra of a concentration series of MEA solutions (1 M, 5 M, and 10 M MEA in H<sub>2</sub>O) at the air/water interface in ssp-polarization. Spectra probe both the (a) stretching and (b) bending regions. The VSF spectrum of the neat air/water interface is shown for reference in grey. In both the stretching and bending regions of the water spectrum, characteristic modes are shown that agree well with the extensive literature of this interface.<sup>37,40,41,43,62,63</sup> In the stretching region, intensity due to water's free OH oscillators (~3700 cm<sup>-1</sup>) as well as a broad feature (<3600 cm<sup>-1</sup>) due to a continuum of

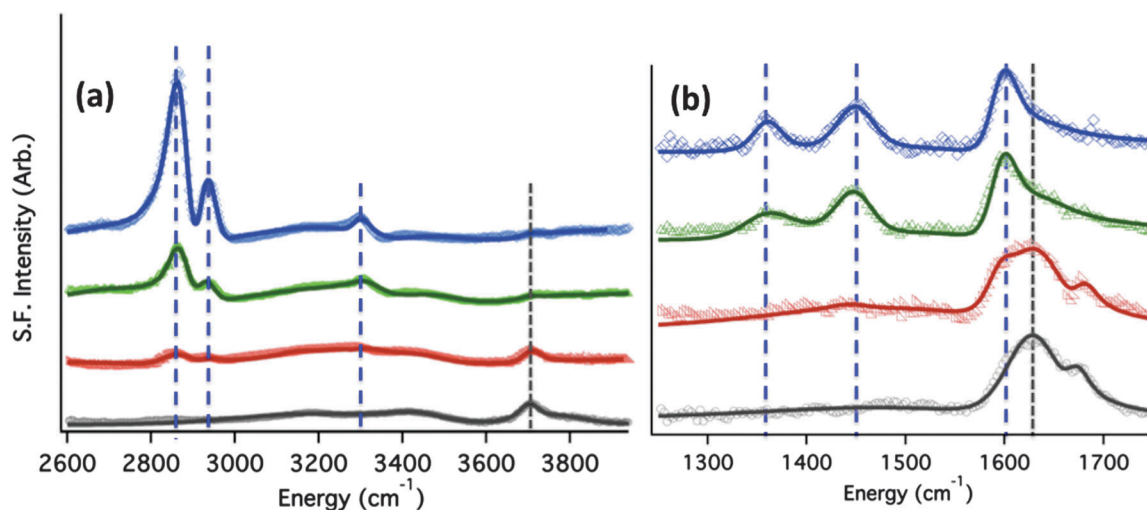
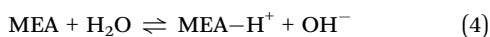


**Fig. 2** VSF spectra of aqueous monoethanolamine solutions at the air–water interface acquired using the ssp-polarization scheme in the (a) CH/OH stretching region and the (b) CH/OH bending region. Experimental data (open shapes) and corresponding fits (solid lines) for neat water (grey) and 1 M (red), 5 M (green), and 10 M (blue) MEA solutions are shown. Incident beam angles were 45° (visible) and 60° (IR). Spectra are offset for clarity, with guide lines for the MEA peaks (blue) and water peaks (grey).

more coordinated water oscillators is present. In the bending region modes due to water's free OH ( $\sim 1625\text{ cm}^{-1}$ ) and more coordinated water oscillators ( $\sim 1740\text{ cm}^{-1}$ ) are present.

Upon introducing MEA to solution, vibrational signatures characteristic of solvated MEA's  $\text{NH}_2$  and  $\text{CH}_2$  stretches ( $\sim 3300\text{ cm}^{-1}$ ,  $\sim 2936\text{ cm}^{-1}$  and  $\sim 2873\text{ cm}^{-1}$ ) and their associated bends ( $\sim 1600\text{ cm}^{-1}$ ,  $\sim 1450\text{ cm}^{-1}$  and  $\sim 1360\text{ cm}^{-1}$ ) appear above the water structure. These new modes are present at all measured concentrations of MEA, showing MEA to not only be present at the surface but also ordered, as the relationship in eqn (2) details.

In addition to solvated MEA contributing intensity to the VSF spectra, reaction products between water and MEA could also affect the spectral shape and deserve consideration. An equilibrium between MEA and its protonated form,  $\text{MEA-H}^+$ , exists in water according to eqn (4), with a  $\text{p}K_a$  of 9.55.<sup>19</sup>



However, at the experimental pH ( $\sim 12.5$ ) the concentration of  $\text{MEA-H}^+$  ( $\sim 9 \times 10^{-8}\text{ M}$ ) is considered negligible. Additionally, protonation of amines is known to have a dramatic effect on the VSF spectral shape;<sup>64</sup> yet no such effect was observed in these spectra. Therefore contributions from  $\text{MEA-H}^+$  species to the VSF spectral shape have been neglected in this study.

All MEA spectra have been globally fit, and achieved a reasonable match at all concentrations without allowing number of peaks, peak position, phase, or broadening to vary. The only fitting parameter that needed varying was the peak amplitude. This suggests that changes in VSF intensity are correlated with changes in bulk solution concentration. Whether these changes in bulk solution concentration result in increased surface population or reorientation of surface species—since VSF intensity arises from a convolution of both—remains, and a full analysis of these effects follows shortly.

**VSF spectral assignments.** In the stretching region of the vibrational spectrum, six peaks arise above the background water spectrum and are due to MEA's methylene and amine groups. The experimental VSF spectra have been fit to peaks at  $2845\text{ cm}^{-1}$ ,  $2873\text{ cm}^{-1}$ ,  $2920\text{ cm}^{-1}$ ,  $2936\text{ cm}^{-1}$ ,  $3300\text{ cm}^{-1}$  and  $3359\text{ cm}^{-1}$ ,

as listed in Table 1. A peak at  $3170\text{ cm}^{-1}$  was also found to be necessary in the global fit, but this mode only contributed appreciable intensity in the 1 M MEA spectra. As VSF intensities depend upon vibrational transitions being both IR and Raman active, bulk IR and Raman studies are often used to guide identification of peaks in VSF spectroscopy. Thus, bulk IR and Raman studies of MEA have been examined to help identify the peaks in these VSF spectra. Knop, *et al.* and Jackson, *et al.* both report FTIR for neat MEA, attributing peaks at  $\sim 3290\text{ cm}^{-1}$  and  $\sim 3354\text{ cm}^{-1}$  to MEA's amine SS- $\text{NH}_2$  and AS- $\text{NH}_2$ , respectively.<sup>48,65</sup> Additionally, peaks at  $2864\text{ cm}^{-1}$  and  $\sim 2930\text{ cm}^{-1}$  are attributed to the  $\text{CH}_2$  stretching bands; the peak at  $3180\text{ cm}^{-1}$  is attributed to MEA's alcohol OH stretch. However, the stretching vibrational modes of MEA, especially those associated with the amine and alcohol groups, are expected to red shift upon dilution with water due to solvation of MEA and subsequent loss of MEA dimers present in neat solutions.<sup>66</sup> Raman frequencies were reported by Samarakoon, *et al.* for  $\sim 3\text{ M}$  MEA solutions.<sup>67</sup> They report peaks at  $3313\text{ cm}^{-1}$ ,  $2952\text{ cm}^{-1}$ ,  $2940\text{ cm}^{-1}$  and  $2884\text{ cm}^{-1}$ , but do not assign the spectra.

Based off these literature peak positions and assignments, it thus follows that the peaks observed in VSF spectra at  $3359\text{ cm}^{-1}$  and  $3300\text{ cm}^{-1}$  are the AS- $\text{NH}_2$  and SS- $\text{NH}_2$  modes, respectively. The broad peak at  $3170\text{ cm}^{-1}$  is the solvated OH mode of MEA; however, due to hydrogen bonding as well as spectral coherence with water's OH modes, its spectral intensity is diminished for all MEA concentrations above 1 M. The modes at  $2936\text{ cm}^{-1}$ ,  $2920\text{ cm}^{-1}$ ,  $2873\text{ cm}^{-1}$ , and  $2845\text{ cm}^{-1}$  are the  $\text{CH}_2$  stretching modes of the methylene backbone. The literature alone does not enable complete assignment for all four  $\text{CH}_2$  modes. Fortunately, due to different polarization selection rules for the methylene SS and AS modes, polarization analysis can be exploited to aid in assigning experimental peaks.<sup>68,69</sup>

As outlined by Lu, *et al.* comparison of ssp and sps relative peak intensities allow for mode assignments of methylene peaks to be made.<sup>69</sup> Fig. 3 shows ssp and sps spectra for 10 M MEA solution in the CH stretching region. Vertical lines act as guides to identify CH intensity due to peaks fit at  $2936\text{ cm}^{-1}$ ,  $2920\text{ cm}^{-1}$ , and  $2873\text{ cm}^{-1}$ . One methylene selection rule states that the

**Table 1** Frequencies and assignments of peaks from experimental and calculated ssp VSF spectra. Experimental frequencies are from global fits of ssp spectra taken at incident angles  $45^\circ$  (visible) and  $60^\circ$  (IR). Calculated frequencies are anharmonic VPT2 frequencies calculated at the B2PLYP/6-311++G(2d,2p) level of theory

Experimental frequencies ( $\text{cm}^{-1} \pm 10\text{ cm}^{-1}$ )	Calculated Frequencies ( $\text{cm}^{-1}$ )	Assignment (mode)
1360	1400, 1376	$\text{CH}_2$ wag (+ $\text{NH}_2$ )
1448	1517, 1497, 1428	$\text{CH}_2$ wag (+ $\text{NH}_2$ )
1595	1614	$\text{NH}_2$ scissor
2845	2814	SS- $\text{CH}_2$
2873	2827	SS- $\text{CH}_2$
2920	2916	AS- $\text{CH}_2$
2936	2968	AS- $\text{CH}_2$
3170	3556	OH stretch
3300	3340, 3391	SS- $\text{NH}_2$
3359	3425	AS- $\text{NH}_2$

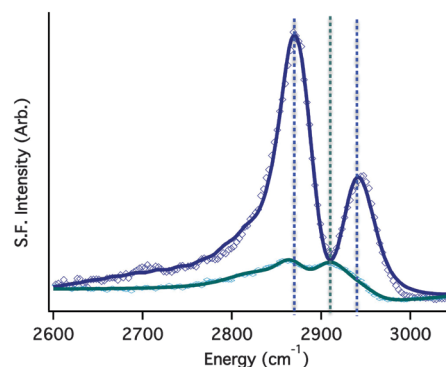


**Fig. 3** VSF spectra of 10 M MEA solutions in ssp- (purple, diamonds) and sps-polarization (teal, circles) in the CH stretching region. Experimental data (open shapes) and corresponding fits (solid lines) are shown. Incident beam angles were  $63^\circ$  (visible) and  $55^\circ$  (IR).

SS-CH<sub>2</sub> and AS-CH<sub>2</sub> modes should be out of phase in ssp spectra. Indeed, as confirmed by the spectral fits of Fig. 3, the peaks at 2873 cm<sup>-1</sup> and 2920 cm<sup>-1</sup> are opposite phases. Additionally, the peak at 2920 cm<sup>-1</sup> in ssp has a higher fitted amplitude than the same peak in ssp. The methylene group selection rules dictate the peak at 2920 cm<sup>-1</sup> should therefore be the AS-CH<sub>2</sub> mode; thus making the peak at 2873 cm<sup>-1</sup> the SS-CH<sub>2</sub> mode. Unfortunately, these selection rules alone have been unable to enable assigning the remaining methylene modes. The selection rules are based on molecular symmetry arguments and assume the methylene backbone of MEA is uncoupled from the motion of the rest of the molecule. This last assumption is not well-satisfied for MEA, as its functional groups can alter the coupling between the methylene stretches.

Similar analysis—taking into account spectral fitting and literature precedent—has been conducted for MEA in the bending region of the vibrational spectrum. As listed in Table 1, three peaks have been uniquely fit to MEA in the bending region: at 1595 cm<sup>-1</sup>, 1448 cm<sup>-1</sup>, and 1360 cm<sup>-1</sup>. FTIR studies report peaks at 1645 cm<sup>-1</sup> and ~1600 cm<sup>-1</sup> assigned to NH rocking.<sup>65,70</sup> Peaks at ~1450 cm<sup>-1</sup> and ~1360 cm<sup>-1</sup> appear in the reported spectra, but are either unassigned or assigned to the methylene bend or C-O-H bend.<sup>65</sup> Unfortunately, as the bending region of the vibrational spectrum is examined much less than the stretching region, few other sources exist to help identify peaks in this region. In fact to our knowledge, only two recent VSF studies report on the bending region of the vibrational spectrum.<sup>43,63</sup>

Thus, a further examination of the spectral peaks in the bending region has been conducted by examining 10 M MEA in D<sub>2</sub>O. D<sub>2</sub>O readily exchanges with the amine group at the pH under study (pH ~ 12.5) but should have marginal effect on the methylene backbone. Indeed, as shown in Fig. S4 (ESI<sup>†</sup>), the 10 M MEA in D<sub>2</sub>O shows a loss of the peak at 1595 cm<sup>-1</sup>, but retention of the peaks at 1448 cm<sup>-1</sup> and 1360 cm<sup>-1</sup>, indicating that the latter two peaks are due to CH<sub>2</sub> modes. Thus, modes in the bending region have been assigned as follows: the peak at 1595 cm<sup>-1</sup> is the NH<sub>2</sub> bend, and the peaks at 1448 cm<sup>-1</sup> and 1360 cm<sup>-1</sup> are CH<sub>2</sub> bends, as shown in Table 1.

### 3.2 Comparison of experimental and calculated VSF spectra

To resolve any remaining uncertainty in the experimental spectral assignments, DFT at the B2PLYP/6-311G++(2d,2p) level of theory has been used to calculate VSF spectra. Reasonable surface spectra were calculated from static gas phase DFT structures that had been matched to surface conformers from the MD simulations. Assignments of the MD conformers to DFT structural “groups” were based on assigned ranges of specific dihedral angles, with DFT structures corresponding to maxima in the dihedral distribution of the MD conformers. A table of the dihedral angles of the DFT structures and the corresponding ranges of the MD conformers has been included in the ESI,<sup>†</sup> along with a discussion of the dihedral assignments and the correlated MD dihedral distributions.

The resultant calculated VSF spectra (orange) are shown in Fig. 4 along with the experimental spectra (blue) for comparison. Peak positions are listed in Table 1. Note the calculated VSF spectra do not include solvent contributions; red shifting of the calculated peak frequencies for MEA's amine and alcohol stretching modes is expected if solvation effects were included. Additionally, intensity from water OH modes as well as coherence effects of the water modes with neighboring MEA modes have not been captured in these calculations.

Fig. 4(b) shows good agreement in both relative peak intensity and peak position for the CH stretching region. In this region, the solvent effects are small leading to the average deviation ( $\pm\sigma$ ) in peak position of ~21 cm<sup>-1</sup>. This small deviation in peak position not only indicates the CH region is favorable for calculating spectra when solvent effects are neglected, but also indicates strong agreement in peak frequencies exists between the experimental and DFT-derived spectra. This strong agreement validates the computational methodology used and lends confidence to the surface behavior information, as well as spectral assignments, extracted from the computational work.

However, Fig. 4(a) and (c) indicate that solvent contributions do play a large role in shaping the VSF spectra in regions where H-bonding plays a larger role, such as the water bending and NH stretching regions. The background water structure greatly impacts the shape of the experimental VSF spectra, resulting in

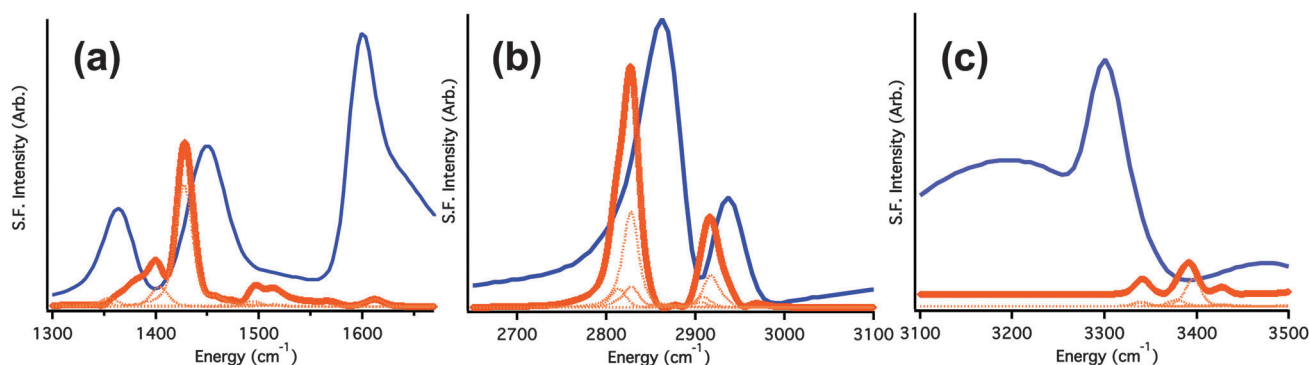


Fig. 4 VSF spectra in ssp-polarization taken experimentally (blue) and calculated (orange) in (a) the bending region, (b) the CH stretching region, and (c) the NH stretching region. Note, the y-axes for (a), (b), and (c) are not comparable, but are different ranges so that calculated spectra may be observed. Dotted orange lines represent conformer contributions to the overall calculated VSF spectra.

greater mismatch between experiments and calculation for Fig. 4(a) and (c). This mismatch is a consequence of the methodology used to calculate the spectra which does not include contributions from the solvent. Not only do the water OH modes greatly contribute intensity to the overall experimental line shape in Fig. 4(a) and (c), but the solvation of MEA's functional groups lead to frequency shifts and spectral broadening of MEA's NH and OH modes. For example, the deviation in peak position between the calculated and experimental fit value of the NH stretching region is  $\sim 52 \text{ cm}^{-1}$ ; the relative intensities are also clearly different between the calculated and experimental spectra in this region. Improvements to the methodology are currently underway to address these issues and better capture the influence of solvation. Indeed, preliminary DFT calculations including explicit solvation (not shown) strongly suggest that the majority of the discrepancies in vibrational frequencies arise from solvation effects. Yet, NH stretches in amines and amides are notoriously difficult to accurately calculate with DFT, and are greatly influenced by solvent effects,<sup>71-73</sup> indicating the  $\sim 52 \text{ cm}^{-1}$  deviation in peak position is not unreasonable. Nevertheless, the CH stretching region of Fig. 4(b) shows good agreement between the calculated and experimental spectra, enabling better interpretation and assignments of vibrational modes there.

In fact, the DFT calculations show coupling between the methylene backbone modes, as suggested by the polarization study of Fig. 3. For example, the assignment of the peak at  $2873 \text{ cm}^{-1}$  in the VSF spectra is SS-CH<sub>2</sub> based off of literature precedent and polarization rules. In the calculated spectra, this peak appears at  $2827 \text{ cm}^{-1}$  and arises instead from coupling between the two methylene units: a strong SS-CH<sub>2</sub> contribution from one and a weaker AS-CH<sub>2</sub> contribution from the other. This coupling behavior has been found to be characteristic for all the methylene stretches and bends calculated, and questions the assumption that each vibrational mode is discretely symmetric or asymmetric. Therefore, mode assignments in Table 1 have been made taking into consideration the various strengths of these coupled vibrations, along with the literature assignments and polarization analysis presented above.

The calculated VSF spectra in the bending region in Fig. 4(a) show good agreement in peak position with the experimental spectra, with an average deviation in peak position of  $\sim 25 \text{ cm}^{-1}$ . However, the relative intensities of the calculated spectra when compared to the experimental spectra are markedly different. Chiefly, this mismatch occurs as a result of the NH<sub>2</sub> scissor/bending mode that appears as a small peak at  $1614 \text{ cm}^{-1}$  in the calculated spectra but is a large peak in the experimental spectra. In the experimental spectra, the intensity from  $1550\text{--}1700 \text{ cm}^{-1}$  has been fit to a single peak due to MEA (at  $1595 \text{ cm}^{-1}$ ) and two peaks due to the nearby water bend. As was the case in the stretching region, the solvent effects on the amine group play a dramatic role in overall experimental VSF spectral line shape. This is additionally observed around  $1500 \text{ cm}^{-1}$ , where the calculated spectra show distinct CH<sub>2</sub> peaks but the experimental spectra show a smooth shoulder due to contributions from nearby water modes. If only the methylene groups' bending

intensities are considered ( $<1520 \text{ cm}^{-1}$ ), the calculated spectra agree with the experiment.

### 3.3 Surface population analysis

As mentioned previously, VSF intensity is due to both surface population and molecular orientation of surface species. Thus in order to fully interpret changes to VSF signal, changes to the surface population and molecular orientation of MEA also require investigation. The surface activity of MEA has been the subject of previous study,<sup>74-77</sup> since its surface presence affects macroscopic parameters such as gas phase transfer rates and solution dynamics. MEA's surface population has been investigated here in order to accurately interpret VSF spectra and to gain a complete picture of MEA's surface adsorption.

**3.3.1 Surface pressure and adsorption calculations.** Equilibrium surface tension values have been obtained for aqueous MEA solutions (ranging from 0.5 M to pure MEA). Surface tensions have been converted to surface pressures,  $\pi$  (the difference between the solution surface tension and the surface tension of neat water), and have been plotted as a function of bulk MEA concentration in Fig. S6(a) (ESI†). The use of surface pressure values facilitates comparison across data sets but, like surface tension, also reflects surface population. The surface pressure isotherm of MEA shows increases in surface pressure track increases in bulk concentration, indicating MEA is surface active. These values compare with the trend reported by Vázquez, *et al.*,<sup>74</sup> considering differences in solution temperature between the two studies.

Both the minimum average surface area per molecule and the overall surface mole fraction have been calculated from the surface pressure values using the Gibbs adsorption equations, as outlined in the ESI.† For these calculations, bulk concentrations of MEA have been corrected with activity coefficients reported by Hilliard.<sup>78</sup> The minimum average surface area per molecule has been calculated to be  $\sim 126 \text{ \AA}^2$  per molecule. This large interfacial footprint is characteristic of other doubly functionalized molecules<sup>53</sup> and indicates MEA is on average largely isolated from itself at the surface, even at high concentrations. Additionally, the overall surface mole fraction of a 10 M MEA solution has been calculated to be  $\sim 0.3$ , roughly equivalent to  $\sim 9.8 \text{ M}$ . For a 5 M solution, the surface mole fraction has been calculated to be  $\sim 0.1$ , roughly equivalent to  $\sim 4.9 \text{ M}$ . These surface mole fractions indicate a fairly large surface density of MEA that roughly mirrors the bulk solution concentration. Taken together, the minimum average surface area per molecule and surface mole fraction suggest MEA occupies a large interfacial footprint with surface population closely tracking bulk solution concentration.

**3.3.2 Density profiles.** Surface population has also been examined through density profile calculations. The density profile extracted from the molecular dynamics simulation of a  $\sim 10 \text{ M}$  MEA solution (160 molecules) is shown in Fig. 5, and may be used to compare the interfacial picture developed from the surface pressure analysis with those from the simulated interfaces.

Fig. 5 shows density in the "bulk" (depths  $>15 \text{ \AA}$ ) for the  $\sim 10 \text{ M}$  MEA solution to be  $\sim 1.01 \text{ g mL}^{-1}$ . This value corresponds well with densities measured experimentally.<sup>79,80</sup> At the surface,

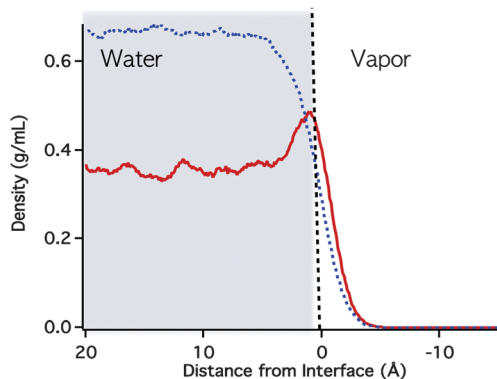


Fig. 5 Density profile of water (blue dotted line) and  $\sim 10$  M MEA (red solid line) extracted after 52 ns of simulation time. The dotted vertical line indicates the interface.

the density of the solution decreases to  $0.93 \text{ g mL}^{-1}$ , but displays enhancement of MEA density relative to the bulk solution. This MEA surface enhancement appears contrary to the surface mole fraction calculated earlier, which suggested surface population of MEA roughly mirrors the bulk population. To investigate this discrepancy the surface mole fraction may be calculated from the density profiles, but only if rigorous accounting of the surface depth has been considered.

The computational surface analysis here, based on the Gibbs dividing surface, however, can be misleading and fail to accurately capture interfacial components. Recent computational work has sought to address these shortcomings of the Gibbs surface definition,<sup>81–85</sup> but issues regarding how to define the thickness of the surface layer, how surface behavior manifests on bulk behavior, and how changing composition reflects changes in interfacial thickness persist.<sup>86,87</sup> Within the community, the definition of the “surface” can range from 2 angstroms<sup>85,88</sup> to a nanometer,<sup>89,90</sup> with results between surface techniques (*i.e.* computed surfaces *vs.* surface tensiometry) varying due to different probe depths.

Nevertheless, for VSF analysis a surface region is generally considered. From a regional approximation of Fig. 5 ( $\pm 3$  Å from the Gibbs dividing surface), the average surface mole fraction is found to be  $\sim 0.267$  (or  $\sim 9$  M), roughly similar to that found in the surface pressure analysis, acknowledging the shortcomings of the interfacial definitions used.

Thus density profiles extracted from MD simulations together with experimental surface pressure measurements show MEA is concentrated at the solution interface, displaying surface activity and a population similar to the overall bulk. Therefore, intensity changes to the VSF spectra in Fig. 2 likely result from increasing surface concentration that tracks with increasing bulk concentration, as shown by the surface pressure and density profile results. Nevertheless, fully understanding MEA’s surface behavior and fully interpreting changes to the VSF spectra requires an understanding of MEA’s surface molecular orientation.

### 3.4 Molecular orientational analysis

As a final examination of the surface behavior of aqueous MEA, molecular orientational analysis has been conducted both

computationally and experimentally. In tandem with the surface population results above, the surface orientational analysis allows for accurate interpretation of the reported VSF spectra but also aids in developing the overall picture of MEA at the surface.

**3.4.1 Orientational analysis *via* molecular dynamics simulations.** Angular distributions extracted from the molecular dynamics trajectories report the average molecular tilt of bonds relative to the surface normal, giving information on MEA’s surface orientation. Correlating the angular distributions of one bond relative to the other gives a sense for not only the orientation of the molecule relative to the surface but also the internal conformation the molecule adopts at the surface. Thus, an analysis of the correlated angular distributions of  $\sim 10$  M MEA has been undertaken in order to understand MEA’s surface orientation; representative distributions are shown in Fig. 6 and 7.

In Fig. 6, the angular distribution of the CO bond relative to the surface normal ( $\theta$ ) has been plotted as a function of the angular distribution of the CN bond relative to the surface normal ( $\phi$ ). The z-axis denotes population, with cooler colors (blue-green) denoting lower percentages of the population and warmer colors (yellow-red) denoting higher percentages of the population. In the bulk (depths  $> 15$  Å; top plot), the correlated angular distribution of the backbone is isotropic. At the surface (0 Å; bottom plot), however, a single, strong maxima appears. This strong maxima is characteristic of not only the top-most

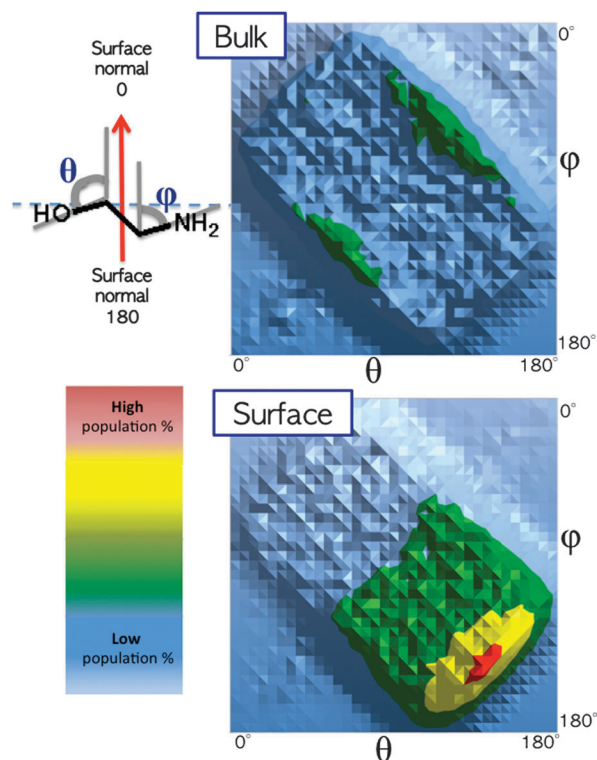


Fig. 6 Correlated angular distributions in the bulk and surface region of  $\sim 10$  M MEA probing the backbone orientation ( $\theta$  *vs.*  $\phi$ ). The color guides on the left describe the z-axis, where cooler colors equate to lower percentage of total population while warmer colors equate to higher percentage of total population.

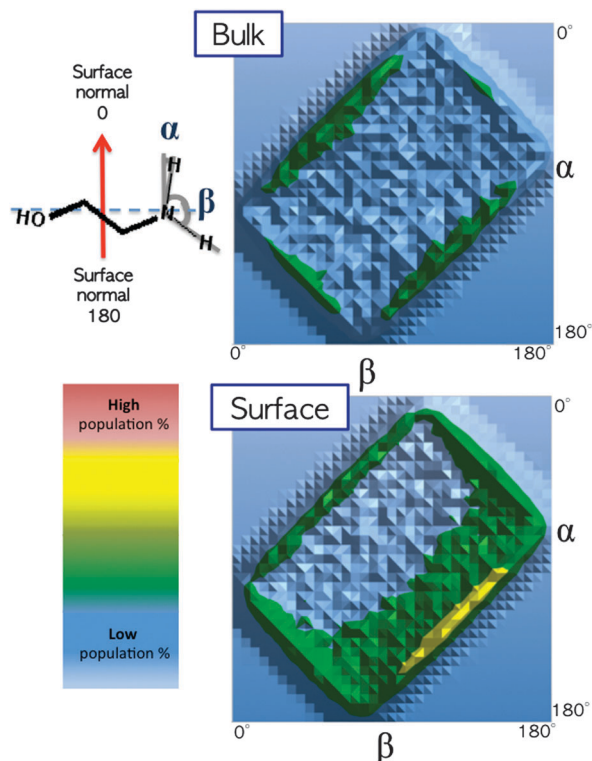


Fig. 7 Correlated angular distributions in the bulk and surface region of  $\sim 10$  M MEA probing the  $\text{NH}_2$  orientation ( $\beta$  vs.  $\alpha$ ). The color guides on the left describe the z-axis, where cooler colors equate to lower percentage of total population while warmer colors equate to higher percentage of total population.

surface at  $0 \text{ \AA}$ , but for the surface region at depths  $\pm 3 \text{ \AA}$  from the defined surface; only the  $0 \text{ \AA}$  plot is shown here for clarity. The correlated angular distribution in the surface region shows a favored orientation of MEA, where the majority of MEA molecules adopt angles of  $\theta$  and  $\phi$  near  $\sim 140^\circ$ . These angles for  $\theta$  and  $\phi$  indicate both CO and CN bonds are pointing into the bulk. Additionally, this combination of angles corresponds to a gauche conformation of MEA's backbone at the surface. The gauche conformation of MEA is not wholly unexpected, as MEA has been shown to exist in the gauche conformation in neat solutions.<sup>66</sup> Integrating over the 2-D surface in the bottom plot of Fig. 6 confirms this picture, and shows  $\sim 98\%$  of the population exists in the gauche conformation at the surface.

Similarly, in Fig. 7 the angular distribution of one NH bond relative to the surface normal ( $\beta$ ) has been plotted as a function of the angular distribution of the other NH bond relative to the surface normal ( $\alpha$ ). Again, the z-axis denotes population, ranging from low percentages (cool colors) to high percentages (warm colors). For both bulk and surface regions, the  $\text{NH}_2$  headgroup is fairly isotropic across the orientational space. However, in the surface region there is a small maxima corresponding to angles of  $\alpha$  and  $\beta$  roughly around  $\sim 110\text{--}140^\circ$ . This indicates that at the surface the  $\text{NH}_2$  group tends to favor both NH bonds pointing into the bulk water. Such an orientation would allow the  $\text{NH}_2$  lone pair to be more open at the surface to attack gas phase  $\text{CO}_2$ , indicating a possible route for surface chemistry.

Similar analysis of all the bond angles of MEA extracted from the MD shows that surface-adsorbed MEA at  $\sim 10$  M adopts a constrained gauche conformation with its  $\text{CH}_2$  groups pointing into the vapor phase and its amine and alcohol headgroups pointing into the bulk. Analysis of the MD simulations with  $\sim 5$  M MEA solution (not shown) shows a similar orientation. Therefore, the behavior of MEA in the MD simulations indicates MEA surface orientation is not sensitive to concentration (at least within the high concentration regime in these studies), supporting the previous interpretation that changes to the VSF spectra in Fig. 2 are largely a result of changing surface population.

#### 3.4.2 Orientational analysis via VSF polarization studies.

Polarization analysis of the experimental VSF spectra provides an additional means of extracting surface orientation information, complementing the MD analysis above. VSF intensity ratios have been used to extract average orientational angles by following an analysis of the functional groups' polarization selection rules and rigorous normalization of spectra. The polarization selection rules of the methylene group have been extensively outlined<sup>68,69,91</sup> and have previously been applied to calculate the average tilt angle of the  $\text{CH}_2$  group relative to the surface normal.<sup>64,68,69</sup> Following similar methodology, analysis of the methylene stretches has been undertaken here, and compared to the orientational information from the molecular dynamics simulations.

Based on the SS- $\text{CH}_2$  and AS- $\text{CH}_2$  ratios in ssp-polarization mentioned above and detailed in the ESI,<sup>†</sup> the average tilt angle of the methylene group in a 10 M MEA solution has been found to be  $46 \pm 6^\circ$  from the surface normal. Tilt angles have also been calculated for both 5 M and 1 M MEA solutions, and show the same tilt value (within error) as the 10 M solution, indicating again that surface orientation is independent of concentration within the concentration regime studied. These tilt angles for the methylene group are consistent with the overall surface orientation inferred from the MD simulations mentioned above.

To further confirm this match between the calculations and experiment, the angle of the bisector of the methylene group (extracted from MD) has been averaged over all methylene twist angles in both the bulk of a  $\sim 10$  M MEA solution and in the surface region, as shown in Fig. 8. In the bulk, the methylene bisector is isotropic, consistent with the earlier orientational

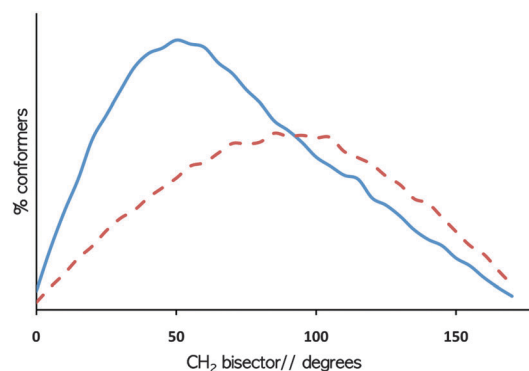


Fig. 8 Angular distribution of  $\sim 10$  M MEA methylene bisector in both the bulk (red dashed) and at the surface (blue solid) averaged over all methylene twists.

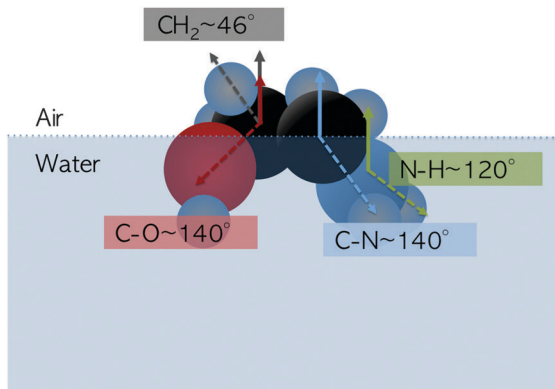


Fig. 9 Generalized picture of MEA's surface orientation and conformation. Representative angles for  $\sim 10$  M MEA solution are shown.

picture developed from the correlated angular distributions in Fig. 6 and 7. At the surface, the methylene groups are preferentially oriented  $\sim 45\text{--}50^\circ$  from surface normal, in agreement with the methylene tilt values found in the VSF polarization studies. Thus polarization analysis of the experimental spectra and the MD simulations confirm the average tilt angle of the methylene groups are  $\sim 46^\circ$  relative to the surface normal at the solution interface.

The orientational analysis of MEA indicates an overall orientation as summarized in Fig. 9, with MEA's methylene backbone pointing into the gas and its functional groups pointing into the bulk. Moreover, MEA favors a gauche conformation independent of concentration, at least in the high concentration regime examined. In light of the surface analyses above, the intensity changes present in the VSF concentration series in Fig. 2 are the result of increasing population at the surface and not changes in surface orientation. This conclusion is also consistent with the large interfacial footprint of MEA ( $\sim 126 \text{ \AA}^2$  per molecule), indicating that even at large surface densities MEA still has sufficient space to adopt a favored orientation.

## 4 Conclusions

As interest in aqueous alkanolamine solutions as sorbents in  $\text{CO}_2$  capture has increased, so has the need to understand the molecular characteristics of the chemical constituents. The results of these studies provide important new insights into the molecular characteristics of MEA at an aqueous surface and how its adsorption at a surface might facilitate  $\text{CO}_2$  capture. The results demonstrate that MEA is present at the surface, and maintains a large interfacial area ( $\sim 126 \text{ \AA}^2$  per molecule) even at high concentrations. Orientational analysis demonstrates that MEA adopts a well ordered gauche conformation at the surface with its methylene backbone oriented toward the vapor phase and its functional groups solvated in the bulk. This surface orientation adopted by MEA may be integral to its surface reactivity, with its  $\text{NH}_2$  lone pair more open to attack gas phase  $\text{CO}_2$ .

Additionally, this work demonstrates the validity of the combined experimental and computational approaches to detail liquid surfaces. The surface population of MEA has been

supported by experimental surface pressure data and computed density profiles from the MD. The surface orientation of MEA has been supported by evaluation of the experimental ssp VSF spectra as well as analysis of the computational MD trajectories. Lastly, comparison of experimental and computational VSF spectra has revealed reasonable agreement with regard to peak positions and relative intensities, especially for the methylene backbone vibrations allowing for confident assignments of spectral modes.

As the most prominent chemical of carbon capture and storage, MEA has long been studied for possible avenues of redesign, acting as a benchmark toward successful innovation. However, as a surface active and soluble molecule, surprisingly little information on MEA's surface properties has been considered during the numerous iterations of novel CCS sorbent materials. This work showcases a robust approach for understanding surface phenomena using a suite of tools necessary for describing interfacial behavior. This work provides a needed picture of MEA surface adsorption and orientation which is required for future investigation into its surface reactivity. Additionally, results from this work indicate the presence of an interface induces an ordering of MEA as well as a preferred conformation. Future designs of CCS sorbents should consider the role of the surface as the need for scalable and highly efficient CCS technology grows. Additionally, as amine scrubbing technology becomes more ubiquitous, the need for information detailing amine surface behavior, especially as it relates to aqueous atmospheric surfaces, will also grow.

## Acknowledgements

The authors thank the National Energy and Technology Laboratory (URS subcontract/task release number RES1100425/005) and the National Science Foundation (CHE-1051215) for supporting this research. Special thanks to Hunaid Nulwala (Carnegie Mellon University) and David Luebke (NETL) for their invaluable assistance and support during this work.

## References

- 1 B. Metz, O. Davidson, H. De Coninck, M. Loos and L. Meyer, *IPCC special report on carbon dioxide capture and storage*, IPCC Technical Report, IPCC Geneva, Switzerland, Cambridge University Press, New York, 2005.
- 2 *International Energy Outlook*, 2014.
- 3 J. D. Figueroa, T. Fout, S. Plasynski, H. McIlvried and R. D. Srivastava, *Int. J. Greenhouse Gas Control*, 2008, **2**, 9–20.
- 4 L. Espinal, D. L. Poster, W. Wong-Ng, A. J. Allen and M. L. Green, *Environ. Sci. Technol.*, 2013, **47**, 11960–11975.
- 5 H. D. Matthews and S. Solomon, *Science*, 2013, **340**, 438–439.
- 6 E. I. Administration, *Annual Energy Review 2011*, DOE/EIA Technical Report DOE/EIA, 0384(2011), Government Printing Office, 2011.
- 7 G. T. Rochelle, *Science*, 2009, **325**, 1652–1654.

- 8 E. Blomen, C. Hendriks and F. Neele, *Energy Procedia*, 2009, **1**, 1505–1512.
- 9 N. McCann, M. Maeder and H. Hasse, *J. Chem. Thermodyn.*, 2011, **43**, 664–669.
- 10 D. Patiño-Echeverri and D. C. Hoppock, *Environ. Sci. Technol.*, 2012, **46**, 1243–1252.
- 11 A. Maiti, *ChemSusChem*, 2009, **2**, 628–631.
- 12 E. I. Privalova, E. Karjalainen, M. Nurmi, P. Mäki Arvela, K. Eränen, H. Tenhu, D. Y. Murzin and J. P. Mikkola, *ChemSusChem*, 2013, **6**, 1500–1509.
- 13 N. A. Valley, E. J. Robertson and G. L. Richmond, *Langmuir*, 2014, **30**, 14226–14233.
- 14 E. J. Robertson and G. L. Richmond, *J. Phys. Chem. C*, 2014, **118**, 28331–28343.
- 15 R. Sedev, *Curr. Opin. Colloid Interface Sci.*, 2011, **16**, 310–316.
- 16 T. Iwahashi, T. Miyamae, K. Kanai, K. Seki, D. Kim and Y. Ouchi, *J. Phys. Chem. B*, 2008, **112**, 11936–11941.
- 17 J. Picálek, B. Minofar, J. Kolafa and P. Jungwirth, *Phys. Chem. Chem. Phys.*, 2008, **10**, 5765.
- 18 J. B. Rollins, B. D. Fitchett and J. C. Conboy, *J. Phys. Chem. B*, 2007, **111**, 4990–4999.
- 19 T. Lewis, M. Faubel, B. Winter and J. C. Hemminger, *Angew. Chem., Int. Ed.*, 2011, **50**, 10178–10181.
- 20 F. Maier, *Angew. Chem., Int. Ed.*, 2011, **50**, 10133–10134.
- 21 I. Niedermaier, M. Bahlmann, C. Papp, C. Kolbeck, W. Wei, S. Krick Calderón, M. Grabau, P. S. Schulz, P. Wasserscheid, H.-P. Steinrück and F. Maier, *J. Am. Chem. Soc.*, 2014, **136**, 436–441.
- 22 C.-C. Lin, W.-T. Liu and C.-S. Tan, *Ind. Eng. Chem. Res.*, 2003, **42**, 2381–2386.
- 23 C.-H. Yu, *Aerosol Air Qual. Res.*, 2012, **12**, 745–769.
- 24 R. Shao and A. Stangeland, *Amines Used in CO<sub>2</sub> Capture*, The Bellona Foundation Technical Report, Oslo, Norway, 2009.
- 25 X. Ge, A. S. Wexler and S. L. Clegg, *Atmos. Environ.*, 2011, **45**, 561–577.
- 26 X. Ge, A. S. Wexler and S. L. Clegg, *Atmos. Environ.*, 2011, **45**, 524–546.
- 27 N. Borduas, J. P. D. Abbatt and J. G. Murphy, *Environ. Sci. Technol.*, 2013, **47**, 6377–6383.
- 28 G. da Silva, *J. Phys. Chem. A*, 2012, **116**, 10980–10986.
- 29 M. C. Facchini, S. Decesari, M. Rinaldi, C. Carbone, E. Finessi, M. Mircea, S. Fuzzi, F. Moretti, E. Tagliavini, D. Ceburnis and C. D. O'Dowd, *Environ. Sci. Technol.*, 2008, **42**, 9116–9121.
- 30 J. Almeida, S. Schobesberger, A. Kürten, I. K. Ortega, O. Kupiainen-Määttä, A. P. Praplan, A. Adamov, A. Amorim, F. Bianchi, M. Breitenlechner, A. David, J. Dommen, N. M. Donahue, A. Downard, E. Dunne, J. Duplissy, S. Ehrhart, R. C. Flagan, A. Franchin, R. Guida, J. Hakala, A. Hansel, M. Heinritzi, H. Henschel, T. Jokinen, H. Junninen, M. Kajos, J. Kangasluoma, H. Keskinen, A. Kupc, T. Kurtén, A. N. Kvashin, A. Laaksonen, K. Lehtipalo, M. Leiminger, J. Leppä, V. Loukonen, V. Makhmutov, S. Mathot, M. J. McGrath, T. Nieminen, T. Olenius, A. Onnela, T. Petäjä, F. Riccobono, I. Riipinen, M. Rissanen, L. Rondo, T. Ruuskanen, F. D. Santos, N. Sarnela, S. Schallhart, R. Schnitzhofer, J. H. Seinfeld, M. Simon, M. Sipilä, Y. Stozhkov, F. Stratmann, A. Tomé, J. Tröstl, G. Tsagkogeorgas, P. Vaattovaara, Y. Viisanen, A. Virtanen, A. Vrtala, P. E. Wagner, E. Weingartner, H. Wex, C. Williamson, D. Wimmer, P. Ye, T. Yli-Juuti, K. S. Carslaw, M. Kulmala, J. Curtius, U. Baltensperger, D. R. Worsnop, H. Vehkamäki and J. Kirkby, *Nature*, 2013, **502**, 359–363.
- 31 J. N. Pitts, Jr, D. Grosjean, K. Van Cauwenberghe, J. P. Schmid and D. R. Fitz, *Environ. Sci. Technol.*, 1978, **12**, 946–953.
- 32 A. G. Lambert, P. B. Davies and D. J. Neivandt, *Appl. Spectrosc. Rev.*, 2005, **40**, 103–145.
- 33 Y. R. Shen, *J. Phys. Chem. C*, 2012, **116**, 15505–15509.
- 34 K. B. Eisenthal, *Chem. Rev.*, 1996, **96**, 1343–1360.
- 35 A. Morita and J. T. Hynes, *Chem. Phys.*, 2000, **258**, 371–390.
- 36 G. L. Richmond, *Chem. Rev.*, 2002, **102**, 2693–2724.
- 37 C. S. Tian and Y. R. Shen, *Chem. Phys. Lett.*, 2009, **470**, 1–6.
- 38 C. D. Bain, P. B. Davies, T. H. Ong, R. N. Ward and M. A. Brown, *Langmuir*, 1991, **7**, 1563–1566.
- 39 F. G. Moore, K. A. Becraft and G. L. Richmond, *Appl. Spectrosc.*, 2002, **56**, 1575–1578.
- 40 E. A. Raymond, T. L. Tarbuck, M. G. Brown and G. L. Richmond, *J. Phys. Chem. B*, 2003, **107**, 546–556.
- 41 E. A. Raymond, T. L. Tarbuck and G. L. Richmond, *J. Phys. Chem. B*, 2002, **106**, 2817–2820.
- 42 V. Ostroverkhov, G. Waychunas and Y. Shen, *Phys. Rev. Lett.*, 2005, **94**, 046102.
- 43 M. Vinaykin and A. V. Benderskii, *J. Phys. Chem. Lett.*, 2012, **3**, 3348–3352.
- 44 S. Woutersen, U. Emmerichs and H. J. Bakker, *Science*, 1997, **278**, 658–660.
- 45 H.-K. Nienhuys, R. A. van Santen and H. J. Bakker, *J. Chem. Phys.*, 2000, **112**, 8487–8494.
- 46 P. R. Monson, S. Patumtevapibal, K. J. Kaufmann and G. W. Robinson, *Chem. Phys. Lett.*, 1974, **28**, 312–315.
- 47 L. Chieffo, J. Shattuck, J. J. Amsden, S. Erramilli and L. D. Ziegler, *Chem. Phys.*, 2007, **341**, 71–80.
- 48 S. Knop, J. Lindner and P. Vöhringer, *Z. Phys. Chem.*, 2011, **225**, 913–926.
- 49 S. N. Wren, N. A. Valley, B. P. Gordon, L. E. McWilliams and G. L. Richmond, *J. Phys. Chem. A*, 2015, **119**, 6391–6403.
- 50 J. T. Davies and E. K. Rideal, *Interfacial Phenomena*, Academic Press, New York, 1963.
- 51 P. G. Blower, S. T. Ota, N. A. Valley, S. R. Wood and G. L. Richmond, *J. Phys. Chem. A*, 2013, **117**, 7887–7903.
- 52 K. L. Plath, N. A. Valley and G. L. Richmond, *J. Phys. Chem. A*, 2013, **117**, 11514–11527.
- 53 N. A. Valley, P. G. Blower, S. R. Wood, K. L. Plath, L. E. McWilliams and G. L. Richmond, *J. Phys. Chem. A*, 2014, **118**, 4778–4789.
- 54 D. A. Case, T. A. Darden, I. T. E. Cheatham, C. L. Simmerling, J. Wang, R. E. Duke, R. Luo, R. C. Walker, W. Zhang, K. M. Merz, B. Robers, S. Hayik, A. Roitberg, G. Seabra, J. Swails, A. W. Gotz, I. Kolossvary, K. F. Wong, F. Paesani, J. Vanicek, R. M. Wolf, J. Liu, X. Wu, S. R. Brozell,

- T. Steinbrecher, H. Gohlke, Q. Cai, X. Ye, J. Wang, M. J. Hsieh, G. Cui, D. R. Roe, D. H. Mathews, M. G. Seetin, R. Salomon-Ferrer, C. Sagui, V. Babin, T. Luchko, S. Gusarvo, A. Kovalenk and P. A. Kollman, *AMBER 12*, University of California, San Francisco, 2012.
- 55 L. Martinez, R. Andrade, E. Birgin and J. Martinez, *J. Comput. Chem.*, 2009, **30**, 2157–2164.
- 56 M. Valiev, E. J. Bylaska, N. Govind, K. Koawlski, T. P. Straatsma, H. J. J. van Dam, D. Wang, J. Nieplocha, E. Apra, T. L. Windus and W. A. de Jong, *Comput. Phys. Commun.*, 2010, **181**, 1477–1489.
- 57 M. J. Frisch, G. W. Trucks, H. B. Schlegel, G. E. Scuseria, M. A. Robb, J. R. Cheeseman, G. Scalmani, V. Barone, B. Mennucci, G. A. Petersson, H. Nakatsuji, M. Caricato, X. Li, H. P. Hratchian, A. F. Izmaylov, J. Bloino, G. Zheng, J. L. Sonnenberg, M. Hada, M. Ehara, K. Toyota, R. Fukuda, J. Hasegawa, M. Ishida, T. Nakajima, Y. Honda, O. Kitao, H. Nakai, T. Vreven, J. A. Montgomery, Jr., J. E. Peralta, F. Ogliaro, M. Bearpark, J. J. Heyd, E. Brothers, K. N. Kudin, V. N. Staroverov, R. Kobayashi, J. Normand, K. Raghavachari, A. Rendell, J. C. Burant, S. S. Iyengar, J. Tomasi, M. Cossi, N. Rega, J. M. Millam, M. Klene, J. E. Knox, J. B. Cross, V. Bakken, C. Adamo, J. Jaramillo, R. Gomperts, R. E. Stratmann, O. Yazyev, A. J. Austin, R. Cammi, C. Pomelli, J. W. Ochterski, R. L. Martin, K. Morokuma, V. G. Zakrzewski, G. A. Voth, P. Salvador, J. J. Dannenberg, S. Dapprich, A. D. Daniels, Ö. Farkas, J. B. Foresman, J. V. Ortiz, J. Cioslowski and D. J. Fox, *Gaussian 09, Revision D.01*, Gaussian Inc., Wallingford, CT, 2009.
- 58 S. Gangarapu, A. T. M. Marcelis and H. Zuilhof, *ChemPhysChem*, 2013, **14**, 3936–3943.
- 59 M. Biczysko, P. Panek, G. Scalmani, J. Bloino and V. Barone, *J. Chem. Theory Comput.*, 2010, **6**, 2115–2125.
- 60 V. Barone, M. Biczysko and J. Bloino, *Phys. Chem. Chem. Phys.*, 2014, **16**, 1759–1787.
- 61 I. Carnimeo, C. Pizzarini, N. Tasinato, P. Stoppa, A. P. Charmet, M. Biczysko, C. Cappelli and V. Barone, *J. Chem. Phys.*, 2013, **139**, 074310.
- 62 R.-r. Feng, Y. Guo, R. Lü, L. Velarde and H.-f. Wang, *J. Phys. Chem. A*, 2011, **115**, 6015–6027.
- 63 Y. Nagata, C.-S. Hsieh, T. Hasegawa, J. Voll, E. H. G. Backus and M. Bonn, *J. Phys. Chem. Lett.*, 2013, **4**, 1872–1877.
- 64 M. Xu, D. Liu and H. C. Allen, *Environ. Sci. Technol.*, 2006, **40**, 1566–1572.
- 65 P. Jackson, K. Robinson, G. Puxty and M. Attalla, *Energy Procedia*, 2009, **1**, 985–994.
- 66 E. F. da Silva, T. Kuznetsova, B. Kvamme and K. M. Merz, *J. Phys. Chem. B*, 2007, **111**, 3695–3703.
- 67 P. A. G. L. Samarakoon, N. H. Andersen, C. Perinu and K.-J. Jens, *Energy Procedia*, 2013, **37**, 2002–2010.
- 68 C. Hirose, H. Yamamoto, N. Akamatsu and K. Domen, *J. Phys. Chem.*, 1993, **97**, 10064–10069.
- 69 R. Lu, W. Gan, B.-H. Wu, H. Chen and H.-f. Wang, *J. Phys. Chem. B*, 2004, **108**, 7297–7306.
- 70 G. Richner and G. Puxty, *Ind. Eng. Chem. Res.*, 2012, **51**, 14317–14324.
- 71 J. Kubelka and T. A. Keiderling, *J. Phys. Chem. A*, 2001, **105**, 10922–10928.
- 72 H. Torii, T. Tatsumi and M. Tasumi, *J. Raman Spectrosc.*, 1998, **29**, 537–546.
- 73 J. A. Grahnen, K. E. Amunson and J. Kubelka, *J. Phys. Chem. B*, 2010, **114**, 13011–13020.
- 74 G. Vázquez, E. Alvarez, J. M. Navaza, R. Rendo and E. Romero, *J. Chem. Eng. Data*, 1997, **42**, 57–59.
- 75 F. Bougie and M. C. Iliuta, *J. Chem. Eng. Data*, 2014, **59**, 355–361.
- 76 S. A. Jayarathna, C. K. Jayarathna, D. A. Kottage, S. Dayarathna, D. A. Eimer and M. C. Melaaen, *J. Chem. Eng. Data*, 2013, **58**, 343–348.
- 77 S. A. Jayarathna, A. Weerasooriya, S. Dayarathna, D. A. Eimer and M. C. Melaaen, *J. Chem. Eng. Data*, 2013, **58**, 986–992.
- 78 M. D. Hilliard, PhD thesis, University of Texas at Austin, 2008.
- 79 R. H. Weiland, J. C. Dingman, D. B. Cronin and G. J. Browning, *J. Chem. Eng. Data*, 1998, **43**, 378–382.
- 80 T. G. Amundsen, L. E. Øi and D. A. Eimer, *J. Chem. Eng. Data*, 2009, **54**, 3096–3100.
- 81 E. Chacon and P. Tarazona, *Phys. Rev. Lett.*, 2003, **91**, 166103.
- 82 M. Jorge, P. Jedlovszky and M. N. D. S. Cordeiro, *J. Phys. Chem. C*, 2010, **114**, 11169–11179.
- 83 M. Jorge, G. Hantal, P. Jedlovszky and M. N. D. S. Cordeiro, *J. Phys. Chem. C*, 2010, **114**, 18656–18663.
- 84 L. B. Pártay, P. Jedlovszky, Á. Vincze and G. Horvai, *J. Phys. Chem. B*, 2008, **112**, 5428–5438.
- 85 A. P. Willard and D. Chandler, *J. Phys. Chem. B*, 2010, **114**, 1954–1958.
- 86 H.-t. Bian, R.-r. Feng, Y.-y. Xu, Y. Guo and H.-f. Wang, *Phys. Chem. Chem. Phys.*, 2008, **10**, 4920–4931.
- 87 W. Hua, X. Chen and H. C. Allen, *J. Phys. Chem. A*, 2011, **115**, 6233–6238.
- 88 M. G. Brown, D. S. Walker, E. A. Raymond and G. L. Richmond, *J. Phys. Chem. B*, 2003, **107**, 237–244.
- 89 S. Roy, S. M. Gruenbaum and J. L. Skinner, *J. Chem. Phys.*, 2014, **141**, 22D505.
- 90 B. Abel, *Annu. Rev. Phys. Chem.*, 2013, **64**, 533–552.
- 91 C. Hirose, N. Akamatsu and K. Domen, *J. Chem. Phys.*, 1992, **96**, 997–1004.